

Article

Not peer-reviewed version

Experimental Investigation of the Interplay of Al-, B-, and Ti-nitrides in Microalloyed Steel and Thermodynamic Analysis

[Markus Führer](#)^{*}, [Sabine Zamberger](#), [Christoph Seubert](#), [Erwin Povoden-Karadeniz](#)

Posted Date: 16 May 2025

doi: 10.20944/preprints202505.1305.v1

Keywords: HSLA; boron-steel; thermodynamics



Preprints.org is a free multidisciplinary platform providing preprint service that is dedicated to making early versions of research outputs permanently available and citable. Preprints posted at Preprints.org appear in Web of Science, Crossref, Google Scholar, Scilit, Europe PMC.

Copyright: This open access article is published under a Creative Commons CC BY 4.0 license, which permit the free download, distribution, and reuse, provided that the author and preprint are cited in any reuse.

Disclaimer/Publisher's Note: The statements, opinions, and data contained in all publications are solely those of the individual author(s) and contributor(s) and not of MDPI and/or the editor(s). MDPI and/or the editor(s) disclaim responsibility for any injury to people or property resulting from any ideas, methods, instructions, or products referred to in the content.

Article

Experimental Investigation of the Interplay of Al-, B-, and Ti-Nitrides in Microalloyed Steel and Thermodynamic Analysis

Markus Führer ^{1,*}, Sabine Zamberger ², Christoph Seubert ¹ and Erwin Povoden-Karadeniz ^{1,3}

¹ Christian Doppler Laboratory for Interfaces and Precipitation Engineering CDL-IPE, Institute of Materials Science and Technology, TU Wien, Getreidemarkt 9, 1060 Vienna, Austria

² voestalpine Forschungsservicegesellschaft Donawitz GmbH, Kerpelystraße 199, 8700 Leoben, Austria

³ Institute of Materials Science and Technology, TU Wien, Getreidemarkt 9, 1060 Vienna, Austria

* Correspondence: markus.fuehrer@tuwien.ac.at

Abstract: Aluminum, boron, and titanium microalloyed into high-strength low-alloy boron steel exhibit a complex interplay, competing for nitrogen, with titanium demonstrating the highest affinity, followed by boron and aluminum. This competition affects the formation and distribution of nitrides, impacting the microstructure and mechanical properties of the steel. Titanium protects boron from forming BN and facilitates the nucleation of acicular ferrite, enhancing toughness. The segregation of boron to grain boundaries, rather than its precipitation as boron nitride, promotes the formation of martensite and thus the through-hardenability. Aluminum nitride is critical in controlling grain size through a pronounced pinning effect. In this study, we employ energy- and wavelength-dispersive X-ray spectroscopy and computer-aided particle analysis to analyze the phase content of 12 high-purity vacuum induction melted samples. The primary objective of this study is to ascertain the dissolution temperatures of nitrides that incorporate Al, B, and Ti. A multicomponent database is constructed through the incorporation of available binary and ternary descriptions, employing the Calphad approach. The findings offer a comprehensive understanding of the relative phase stabilities and the associated interplay among the involved elements Al, B, and Ti in the Fe-rich corner of the system.

Keywords: HSLA; boron-steel; thermodynamics

1. Introduction

High-strength low-alloy (HSLA) boron steels are widely recognized for their enhanced mechanical properties, which are achieved through the precise control of their microstructure [1]. Reaching the full potential of alloying elements in microalloyed steel is dependent on correctly understanding the variables processing, thermodynamics, and kinetics [2] to reach the desired mechanical properties with reasonable costs [1]. The addition of boron to microalloyed steel has been shown to enhance through-hardenability. Furthermore, the formation of bainite and martensite is promoted by the alloying of the steel with only some ten wt.-ppm of boron [3–5]. The phenomenon referred to as the 'boron effect' has been observed to enhance through-hardenability rather than hardness [6]. The underlying mechanism of this advantageous effect involves the retention of boron in solid solution in the matrix, thereby preventing the formation of boron nitride (BN) [7]. In order to protect the steel from the occurrence of this second phase formation, i.e., binding the nitrogen instead of BN, aluminum or titanium are utilized [7]. Titanium, with its highest affinity for nitrogen [8], primarily forms titanium nitrides (TiN), which are known to refine the grain structure and improve toughness [9]. Aluminum nitride (AlN) has been shown to be particularly effective in controlling grain size due to its pronounced pinning effect, which is known to inhibit grain growth [10]. The interplay between these elements and their respective role in the nitride stabilization is critical in

determining the final microstructure and mechanical properties of the steel. The interactive role of Al, B, and Ti for the formation and dissolution of nitride precipitates, as well as the associated content of boron in solid solution for the consolidation of martensite, is a subject of considerable concern [7].

The objective of this study is to apply Calphad [11] in order to elucidate and validate the thermodynamic behavior and microstructural evolution of microalloyed steels containing aluminum, boron, and titanium nitrides in the Fe-rich Fe-Al-B-Ti-C-N system. Experimentally, a combination of advanced analytical techniques, including energy-dispersive X-ray spectroscopy (EDS) in combination with computer-aided EDS, and wavelength-dispersive X-ray spectroscopy is employed to analyze 12 high-purity vacuum-induction melted samples. Furthermore, the material is subjected to annealing under equilibrium-like durations in a dilatometer at varying temperatures. This procedure is employed to ascertain the solvus temperatures of the implicated precipitates. The experimental results are used to validate the accuracy of the integration of binary and ternary reassessments for multi-component microalloyed steel [12–16] in the thermodynamic multi-component database ME-Fe_CDLIPE2.0.2.tdb [17]. Particular emphasis is given on the solvus temperatures (T_{sol}) of the relevant nitrides as a function of varying chemical compositions in the Fe-rich side in diluted systems. We provide an assessed Gibbs-energy description of the BN phase, giving high weight to an accurate solubility description.

It is found that the solvus temperature of BN as a function of the Al fraction is lower than described by available thermodynamic assessments, and ≥ 0.09 wt.-% alloying of Al completely inhibits the formation of BN in the dilute Fe-Al-B-C-N system studied. In the Fe-Al-B-C-N system with approximately 0.09 wt.-% Al, the formation of BN can be completely blocked. Titanium proves to be very efficient in terms of binding nitrogen, with the presence of 0.02 wt.-% Ti completely blocking the formation of AlN and shifting T_{sol} of BN down by 150 °C. At 0.03 wt.-% Ti the formation of BN is completely blocked. In the alloys with even a small amount of Ti, abnormal grain growth behavior [18] is observed. This inhomogeneous grain growth is attributed to the absence of AlN precipitates, which are known to retard grain boundary movement.

The utilization of Al for deoxidation in steel was predominant until the discovery regarding the pivotal influence of AlN precipitates on steel properties. The ability of AlN to impede austenite grain coarsening through the pinning of grain boundaries [19] is well-documented. Conversely, the presence of excessive primary AlN has been shown to induce embrittlement [10,20]. The stoichiometric phase [21] AlN possesses a hexagonal wurtzite structure with a space group of P63mc. Upon cooling, AlN begins to become stable in the austenite (γ) region of microalloyed steel, predominantly nucleating heterogeneously at grain boundaries [10] due to a high volumetric misfit of 70% between the γ -matrix and AlN-precipitate [10,22,23]. In the ferrite (α) phase, the thermomechanical processing route and the nominal Al and N contents [24–27] are pivotal factors in determining the initial phase, representing metastable cubic rock-salt structured AlN, with a size ranging from 5 to 10 nanometers. This metastable AlN can subsequently be converted into the stable hexagonal AlN modification [28].

The „boron effect“ has been demonstrated to be beneficial; however, it only occurs when solute B atoms are present at grain boundaries, which makes the formation of BN a matter of significant concern. BN occurs as hexagonal BN type (Pearson symbol hP4 [29]) in steel [7] and the nucleation of BN has been reported to occur at austenite grain boundaries [30]. The size of the BN precipitates, ranging from 5 to 30 μm , is reported to be dependent on the time-temperature profile of the applied heat treatments [31]. However, this size range is too coarse to have any beneficial effect on the properties of the material [7].

Titanium exhibits a strong affinity for carbon and nitrogen, which leads to the formation of TiN and TiC precipitates. TiN nucleates as face-centered cubic (fcc) phase, often referred to as MX phase, with M being Ti, V, or Nb and X being C and N [2]. The high thermal and chemical stability of the carbonitride results in a high T_{sol} of the precipitates, even at low fractions of Ti [32]. Carbonitrides have been shown to impede grain growth and recrystallization, which in turn alters the

transformation characteristics and improves the properties of the material [9]. The beneficial influence of Ti precipitates is only possible in fully killed steels that have undergone deoxidation with Al due to the strong deoxidizing characteristics and the subsequent formation of titanium oxide [33].

In their study, Wang et al. [8] examined the precipitation of AlN, BN, and TiN in boron-bearing steel from a thermodynamic perspective, concluding that the precipitation of TiN occurs predominantly before BN and AlN. In a related study, Gontijo et al. [34] report on the effects of combined addition of B and Ti in microalloyed steel. The authors find that the formation of TiN is preferential over BN and AlN with regard to ductility behavior. This phenomenon occurs due to segregated B at grain boundaries, which retards the formation of ferrite films at the austenite grain boundaries.

Abnormal grain growth (AGG) in steel is a phenomenon in which certain grains grow significantly larger than others during heat treatment processes such as annealing [18]. This can result in a bimodal grain size distribution that affects the properties of the material. AGG typically occurs in steel at elevated temperatures after the dissolution of precipitates such as Nb or V carbonitrides, which are known to exert a strong solute drag effect on grain boundary mobility [35–37].

2. The Thermodynamics of the Fe-C-N-A-B-Ti System in the Fe-Rich Corner in Microalloyed Steel

Typically, the available binary and ternary phase diagrams of a multi-component system encompass the broad spectrum of compositions well, though they do not concentrate on a specific composition space corner. In the case of microalloyed steel with diluted fractions of certain elements, this can result in substantial discrepancies between the predicted and observed phase stability [38]. It is therefore imperative to accurately delineate the thermodynamics and phase boundaries of the constituent phases within the dilute microalloying range, to ensure the efficacy of thermokinetic simulations with high predictive capabilities. This study employs available thermodynamic descriptions of binary and ternary systems, combining them into a comprehensive thermodynamic database. The objective is to accurately predict the phase stabilities for the Fe-rich side of the multicomponent system Fe-C-N-Al-B-Ti, with a particular focus on the interaction of Al, B, and Ti with nitrogen. It is particularly evaluated in this study, whether the approach of combining binary and ternary thermodynamics, while keeping the further extension to the quaternary and quinary subsystems and beyond ideal (i.e. without additional multi-component excess Gibbs energies optimizations) yields sufficient predictive power for technological alloys, which would be represented by low deviations between experimental data and calculated results.

2.1. Calphad Modeling

For the establishment of the thermodynamic database, the CALPHAD (CALculation of PHase Diagrams) approach [11,39] is used. In multi-component systems, it is essential to characterize the thermodynamics of all lower-order systems accurately. For pure components, the thermodynamic data is taken from Dinsdale [40]. The Redlich – Kister -Muggianu model for the Gibbs excess energy description for the phases liquid (L), bcc_A2 (bcc, ferrite, α -Fe), and fcc_A1 (fcc, austenite, γ -Fe) is used. The liquid phase uses a random substitutional solution model. The phases bcc and fcc are described by a regular solution model. Carbides and nitrides are described with sublattice models. The following section provides a critical review of the composing subsystems.

2.2. Subsystems with Relevance in Microalloyed Steel

Fe-based databases are determined by the binary systems containing Fe, i.e., Fe-C, Fe-N, Fe-B, Fe-Ti, and Fe-Al. Intrinsic stabilities of non-ferrous nitrides and carbo-nitrides are relevant, so the Al-N, Al-C, Al-Ti, Ti-C, Ti-N, and B-N systems are added. The Fe-C system, actually representing the steel matrix for the precipitation, is of significant importance to the iron and steel industry, as evidenced by the extensive reviews conducted [12,41,42]. The assessment by Gustafson [12] has

gained considerable recognition within Calphad databases [43]. In addition to the conventional liquid, bcc, and fcc phases, several iron carbides have been identified, with Fe₃C (cementite) [12,44] being the sole metastable carbide. In fact, competitive nitrogen solubility in iron, versus nitride stabilization, is relevant, and thus also the Fe-N system, with the description by Frisk proving reliable [13]. A similar question concerns boron solubility in the steel matrix, versus boride stabilization, and in this context the Fe-B system, which has been evaluated by various researchers [45–48], with some providing thermodynamic calculations [46,49–51]. The primary difference among models lies in the site of boron dissolution within steel phases. Boron can be considered the smallest substitutional element [14,49], the largest interstitial element [50], or a mixed substitutional-interstitial element in bcc-Fe and fcc-Fe [45,52–54]. Raghavan [55] gives a brief review of experimental data for the extension to the Fe-B-N system. Tomashik [56] provides an up-to-date review of the available data and claims that ternary phases do not occur. Fountain and Chipman [57] demonstrate a decrease in nitrogen solubility with increasing boron content. The Fe-B, Fe-B-N and Fe-B-C system has previously been evaluated and in part re-optimized by the present author [58], determining the influence of boron on the solvus temperature of BN, the liquidus and solidus temperatures of the system. Descriptions for these systems are taken as suggested by Führer et al. [58]. The description for the Al-N system is taken from Saunders [59]. In a recent publication [27], the system Fe-Al-N-C is reassessed for the Fe-rich corner in dilute systems, with particular emphasis on accurate thermodynamic description of the AlN phase. Ti-carbonitrides, which are classified as part of the MX-class [60], are modeled as a FCC solid solution. The model parameters are defined in such a way as to allow for the separation between the austenitic steel phase and the carbo-nitride (MX) - phase in the Fe-base system. The multi-component model is expressed as (Fe, Ti)(C, N, Va) within the compound energy formalism.

The binary subsystem description for Ti-C is adopted from the Matcalc steel database [61]. The parameters for Fe-Ti and Ti-N are taken from Lee [15]. In the context of the simulation, the ternary subsystem that has been determined to be of major importance is composed of Fe-Al-C and Fe-Al-N, as delineated by Chin et al. [16] and Hillert and Jonsson [62]. The ternary extension to Fe-Ti-C system is taken from Jacob et al. [60]. Table 1 provides a summary of the used subsystems for describing the Fe-C-N-Al-B-Ti system.

Table 1. Summary of binary and ternary subsystems used in the present study.

System	Citation
Fe - C	Gustafson [12]
Fe - N	Frisk [13]
Fe - B, Fe-B-C, Fe-B-N	Miettinen and Vassilev [63], Führer et al. [58]
Fe - Al	Seierstein [64], Chin et al. [16]
Fe - Ti	Lee [15]
Ti - N	Lee [15]
Ti - C	Povoden-Karadeniz [61]
Al - Ti	Witusiewicz et al. [65]
Al - N	Saunders [59], Führer et al. [27]
Al - C	Chin et al. [16]
Fe - Al - C	Chin et al. [16]
Fe - Al - N	Hillert and Jonsson [62]
Fe - Ti - C	Povoden-Karadeniz [61]

2.3. Gibbs-Energy Description of the BN-Phase

The solubility product, K , defines the concentration product between B and N in weight percent where BN is dissolved in the steel matrix at a given temperature. Solubility products are then plotted logarithmically, $\log(K)$, as a function of temperature. The lower the $\log(K)$, the lower the respective concentrations of B and N at which all BN is dissolved. Conversely, BN precipitation occurs at higher

concentrations of B and N than given by K. It is self-evident that $\log(K)$ is typically lower at lower temperatures: The phase boundary between the steel matrix phase and the precipitate at low temperatures is usually at more dilute compositions than at higher temperatures. As illustrated in Figure 1, a comparison is presented between the experimentally evaluated solubility products [57,66,67] (full lines) and the calculated ones [68–70] (dotted lines) in the austenite.

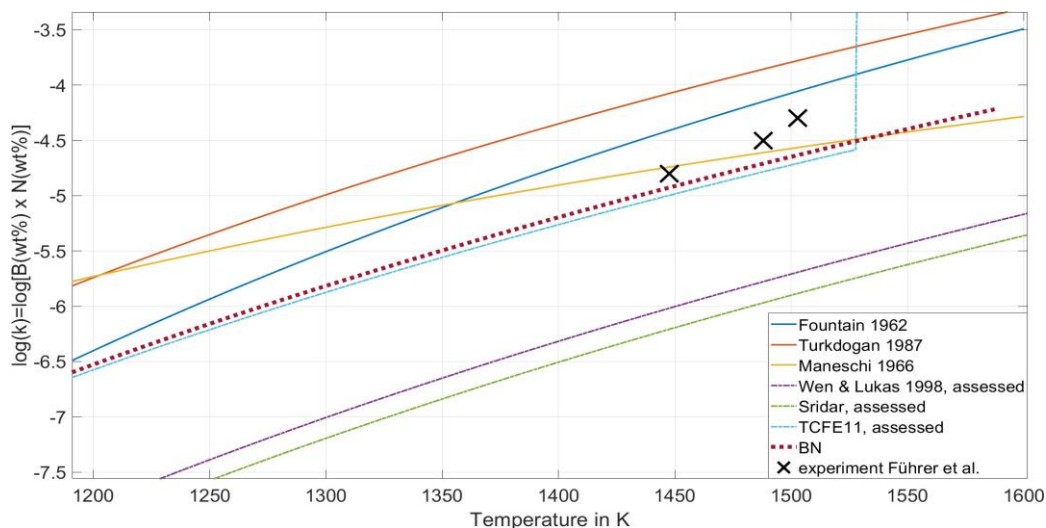


Figure 1. Full and dashed lines show a comparison of solubility products $\log(K) = \log[B(\text{wt.}\%) \cdot N(\text{wt.}\%)]$ in the austenite from experiments from the literature [57,66,67], and assessed thermodynamic descriptions [68–70], respectively. The red dotted line shows the result of the newly assessed description. Black crosses are the experimental results from Führer et al. [58]. (For interpretation of the references to color in this figure legend, the reader is referred to the Web version of this article.)

The available descriptions can be divided into two groups, with higher and lower solubility product values. Führer et al. [58] provide a comprehensive overview of the substantial discrepancy between the two groups. Importantly, the groups are defined by their approach either to correctly describe thermodynamic quantities, i.e., enthalpy of formation ΔH_f , entropy S_{298} , and heat capacity C_{p298} , or correctly depicting solubility limits. Usually, microscopic dissolution observation should be consistent with the thermodynamic properties of a phase, controlling this behavior, as it could be seen for AlN [27]. However, the authors [58] have demonstrated that, in order to accurately depict the phase stability and thermodynamic quantities of the BN phase, it is for consistency between dissolution and thermodynamic properties imperative to take into account the pronounced segregation tendency of B atoms, in conjunction with the Calphad-type thermodynamic description. In this work, an alternative Gibbs-energy description of the BN phase is presented. The objective of this description is to provide a comprehensive characterization of the experimentally accessible solubility products, which sort of involves the pronounced segregation tendency of B atoms, which are illustrated in Eq. 1,

$$G_{Al:N}^{AlN} = -222000 + 45 \cdot T + 7 \cdot T \cdot \ln(T) - 0.002 \cdot T^2 - 3e^{-7} \cdot T^3 + GHSE_{R_N} + GHSE_{R_B} \quad (1)$$

It should be noted that this parameter proposal inevitably leads to different predicted thermodynamics of the BN phase. This results in deviations from the experimental values of Dworkin et al. [71] for enthalpy of formation (ΔH_f), entropy (S_{298}), and heat capacity (C_{p298}) of approximately 25 kJmol⁻¹, 4 Jmol⁻¹K⁻¹ and < 0.1 Jmol⁻¹K⁻¹, respectively. The BN phase is regarded as fully stoichiometric (B)(N). For a more thorough examination of the BN phase description and the deeper discussion of the pertinent subsystems that contain boron, please refer to the extant literature [58,63].

3. Materials and Sample Characterization

3.1. Composition

In the present study, we use the Fe-Al-B-C-N alloying system with 4 and 5 variations of the B and Al contents from 0 to 0.083 wt.-% and 0 to 0.4 wt.%, respectively. In the Fe-Al-B-Ti-C-N system, the Ti microalloying content is varied from 0 to 0.042 wt.-% in four variations. The alloying of the material is carried out with high precision in a vacuum induction melting furnace, followed by a casting and forging process and a homogenizing annealing treatment at 1000 °C for ten hours in a vacuum furnace. The resulting composition of the elements C, Al, B, Ti, Mn, and S is measured by optical emission spectroscopy (OES) and the N fraction by the LECO method [72,73], see Table 2, with an uncertainty of five ppm and seven ppm, respectively. The numbers in the sample designations indicate the boron fraction in wt.-ppm and the Al and Ti fractions in tens of wt.-ppm. The sample geometries are cylindrical with Ø 5 mm and a height of 10 mm for EDS particle analysis. The stability of precipitates, e.g., AlN, in which Al can form oxides, can be influenced to a significant degree by the presence of impurities. Thus, particularly for the case of phase evaluation in microalloying steels, the utilization of vacuum induction melting for sample preparation is mandatory. It has been demonstrated to result in a significant reduction of impurity levels (see Table 2), with oxygen levels measured in parts per million (wt.). Due to the extremely low impurity levels, the influence of impurity elements on the stability of AlN, BN, and TiN is considered negligible.

Table 2. Composition of the via vacuum induction melting produced alloys (wt.%). Numbers in the sample labeling give boron in wt.-ppm and Al and Ti in tens of wt.-ppm.

mass fraction in %, Fe = bal.								
Alloy	C	N	Al	B	Ti	Mn	S	O
Fe-C-N-Al-B - B-variation								
Al29B0	0.51	0.0076	0.029	0.0002	0.000	0.123	0.006	0.001
Al29B22	0.50	0.0073	0.029	0.0022	0.000	0.123	0.006	0.001
Al36B44	0.50	0.0070	0.036	0.0044	0.000	0.123	0.007	0.001
Fe-C-N-Al-B - Al-variation								
B21Al0	0.50	0.0070	0.009	0.0021	0.000	0.115	0.0070	0.001
B19Al35	0.49	0.0079	0.035	0.0019	0.000	0.114	0.008	0.001
B21Al87	0.49	0.0083	0.087	0.0021	0.000	0.114	0.008	0.001
B21Al180	0.50	0.0086	0.180	0.0021	0.000	0.117	0.008	0.001
B21Al416	0.49	0.0086	0.416	0.0021	0.000	0.117	0.009	0.001
Fe-C-N-Al-B-Ti - Ti-variation								
Al36B25Ti0	0.51	0.0069	0.036	0.0025	0.000	0.131	0.007	0.001
Al38B36Ti20	0.50	0.0052	0.038	0.0036	0.020	0.131	0.007	0.001
Al42B38Ti30	0.50	0.0045	0.042	0.0038	0.030	0.131	0.007	0.001
Al44B39Ti42	0.50	0.0042	0.044	0.0039	0.042	0.130	0.007	0.001

3.2. Methods

3.2.1. Microstructure Analysis

The analysis of the resulting microstructures, focusing on AlN, BN, and TiN precipitates, is conducted using a ZEISS SIGMA scanning electron microscope (SEM) equipped with a field emission gun operating at an electron beam voltage of 10 kV and a working distance of 10 mm. The chemical analysis is facilitated by EDS, while wavelength-dispersive spectroscopy (WDS) is employed for elements B and N with a low ordering number. The EDS detector utilized is an Octane elect super with a 70 mm² detector size, while the WDS spectrometer is an EDAX Lambdaplus WDS [74] model. The backscatter electron mode (BSE) in the SEM offers a favorable mass contrast for the precipitates, given their comparatively low atomic masses relative to Fe. For good statistical power, either 50 sections are observed manually in the SEM or computer-aided particle analysis is used. The former austenite grain size is revealed by using the etching reagent PM1998 [75]. The T_{sol} of the precipitates

of the alloys from Table 2 are evaluated by annealing the samples at different temperatures in a Bähr dilatometer type 805 under a vacuum atmosphere with alteration steps of 30 °C for 30 minutes and then quenching down to room temperature to „freeze“ the microstructure. The temperature curve of the heat treatments is shown in Figure 2. It should be noted that unless otherwise specified, all heat treatments are assumed to have undergone heating and cooling rates of 70 K/s and 100 K/s, respectively.

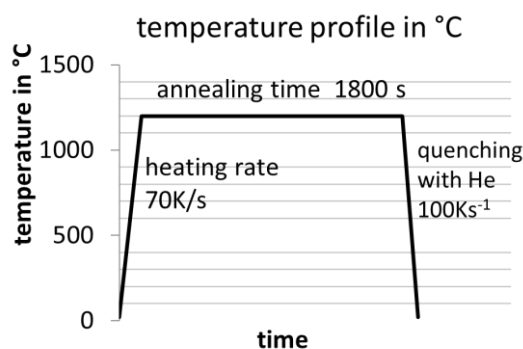


Figure 2. Applied temperature-time profile in a Bähr dilatometer type 805 under vacuum conditions for determining T_{sol} of the nitrides.

3.2.2. EDS - Particle Analysis

In addition to the manual analysis of precipitates in the SEM, the computer-aided EDS particle analysis method (PA) [27] is employed. The analysis is conducted using a JEOL JSM-7800F scanning electron microscope with a field emission gun at an operation voltage of 12 kV and an „Oxford X-MAXN“ EDS detector with a 50 mm² detector size for computer-aided EDS particle analysis (PA). The primary advantage of PA is the acquisition of substantial statistical data concerning precipitates, including their distribution at interfaces, mean particle size and distribution, and phase fractions. Notably, PA effectively addresses the challenge posed by small and sparse precipitates, particularly those of AlN [27]. The evaluation of particles is conducted in accordance with the methodology outlined by Führer et al. [27]. The salient characteristics of this approach are as follows: the lower detection limit is 60 nm, and the determination of particles is facilitated by their chemical composition. However, this approach is encumbered by the difficulty of detecting light elements with EDS, which introduces a degree of uncertainty. In contradistinction, the substantial expanse of the investigative domain, in conjunction with the implementation of automated evaluation methodologies, facilitates the consideration of a considerable array of precipitates. Consequently, this approach engenders the generation of reliable statistics concerning precipitate distributions. The particles are then identified using certain composition boundaries, as outlined in Table 3. For AlN and MnS, the recommendation for the selection limit proposed by Führer et al. [27] is adhered to. The presence of BN is indicated by the detection of boron or nitrogen. The solubility of other elements is minimal, and thus, the detection of BN is a reliable indicator of the presence of these elements. BN contains light elements but possesses a substantial diameter, a property that enables its detection through particle analysis. Given the classification of TiN as a carbonitride, the high solubility of carbon must be considered. Given the fact that carbon and nitrogen are light elements and titanium is more readily detected with EDS, the detection of titanium is sufficient for marking a particle as TiN. Upon the satisfaction of all criteria, the spatial coordinates, mean ECD, surface fraction, and precipitate size distribution of the particles are determined.

Table 3. Selection limits for precipitates AlN, BN, TiN, MnS, and Al₂O₃ after particle analysis. Boundary conditions for elements are given in wt.%.

Type

	ECD [nm]	Al [wt.%]	B [wt.%]	N [wt.%]	Ti [wt.%]	C [wt.%]	Mn [wt.%]	S [wt.%]	O [wt.%]
AlN	> 60	>2	< 0.1	> 0	< 0.1	< 3	< 3	< 0.1	< 0.1
BN	> 60	< 0.1	> 2	> 0	< 0.1	< 3	< 3	< 0.1	< 0.1
TiN	> 60	< 0.1	< 0.1	> 0	> 2	> 0	< 3	< 0.1	< 0.1
MnS	> 60	< 3	< 3	< 3	< 3	< 3	> 3	> 0.5	< 0.1
Al ₂ O ₃	> 60	> 2	< 3	< 3	< 3	< 3	< 3	< 0.1	> 1

4. Results

4.1. Initial Microstructure

Figure 3 shows the microstructure of the alloy with different B fractions after annealing in a vacuum furnace at 1000 °C for 10 hours followed by cooling to room temperature at 90 K/min and etching with Nital. The results clearly demonstrate a correlation between an increase in grain size and an increase in B fraction between 22 and 44 wt. ppm boron alloying. This phenomenon has been well-documented in the literature concerning B-alloyed steel and is attributed to the absence of AlN, which are known for their strong grain boundary pinning force, due to the formation of the more stable BN. Conversely, BN are too coarse to have any influence on grain growth [7]. This indicates that the correct prediction of phase relations is highly relevant for interpretations of the according microstructure.

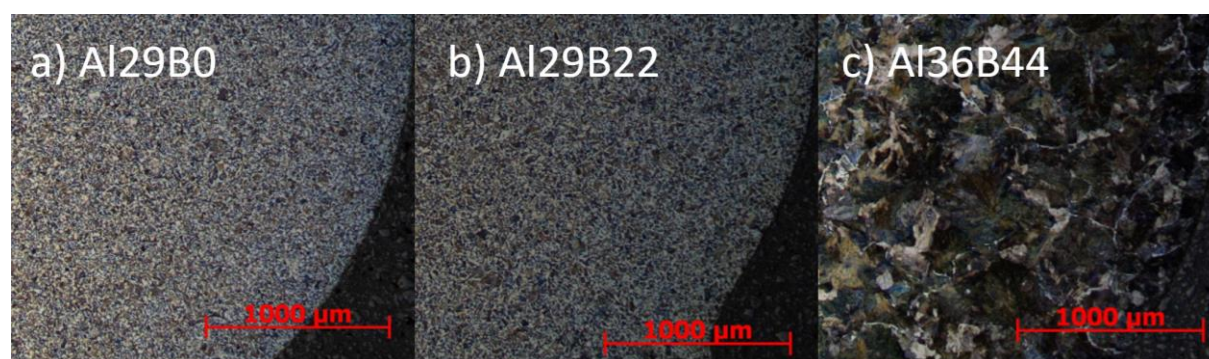


Figure 3. Microstructure of the samples after homogenization annealing in the vacuum furnace at 1000°C for 10 hours and subsequent cooling to room temperature with 90 K/min for the alloys with varying B fraction. Etching agent: Nital 5%. Magnification: x25.

4.2. Interrelation of AlN and BN Within Fe-C-N-Al-B.

4.2.1. Solvus - Temperature of AlN and BN

In Table 4, the experimental results of T_{sol} for AlN and BN precipitates using EDS/WDS analysis after annealing at different temperatures are presented, considering various Al and B concentrations, along with the associated range of error. The assessment of T_{sol} for AlN with low Al fractions and varying B content, i.e., alloys Al29B0, Al29B22, and Al36B44, poses significant challenges due to the low phase fraction and small diameter of AlN [10,27]. Utilizing the outcomes derived from EDS particle analysis and acknowledging the microstructure that has undergone homogenization annealing at 1000 °C (Figure 3 b, c), it can be deduced that T_{sol} of alloy Al36B44 is approximately 970 °C. This determination is substantiated by the considerable augmentation in the affected grain size that has been observed following homogenization annealing, as evidenced by the comparative analysis in Figure 3 (b) and (c). The solubility of BN in the alloys with varying B fraction ranges from 1200 °C to 1215 °C, as BN is present at 1200 °C but not at 1235°C or higher temperatures, in any of the investigated alloys. In alloys with fixed B and varying Al fraction, a decrease in T_{sol} of BN is observed, with complete suppression of BN formation at concentrations greater than 0.9 wt.-%. T_{sol} of AlN at temperatures above 1300 °C (alloys

B21A1180, B21A1416) is associated with a higher degree of uncertainty, primarily due to the challenges associated with conducting heat treatment experiments at such elevated temperatures, particularly the difficulty of achieving stable connection of the thermocouple on the sample surface.

Table 4. Experimental and computed T_{sol} of AlN and BN in the Fe-C-N-Al-B system.

Alloy	Al	B	Ti	N	T_{sol} AlN	T_{sol} BN	T_{sol}	
							in wt.-%	experimental in °C
Al29B0	0.029	0.0002	0.000	0.0076	1150±30	-	1187	-
Al29B22	0.029	0.0022	0.000	0.0073	1150±30	1200±15	1165	1235
Al36B44	0.036	0.0044	0.000	0.0070	970±40	1215±15	1122	1280
B21Al0	0.009	0.0021	0.000	0.0070	-	1230±15	-	1230
B19Al35	0.035	0.0019	0.000	0.0079	1180±20	1215±20	1195	1220
B21Al88	0.088	0.0021	0.000	0.0083	1250±20	1110±20	1280	-
B21A1180	0.180	0.0021	0.000	0.0086	1350±50	-	1370	-
B21A1416	0.416	0.0021	0.000	0.0086	(1450±50)	-	-	1460

For alloys B21A1180 and B21A1416, we therefore employ thermodynamic equilibrium simulation in order to discuss the accuracy of experimentally determined T_{sol} . Figure 4 shows an SE image (a) and the EDS mapping of Al (b) and Mn (c) for alloy B21A188 after annealing at 1100°C for 1800 s. The concentrations of Al in part b reveal the presence of AlN particles with a size in the range of several hundred nanometers.

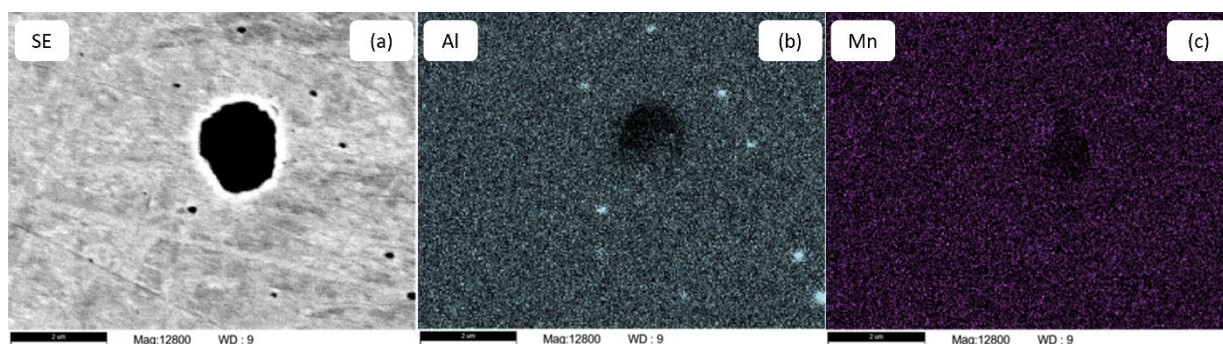


Figure 4. Chemical analysis mapping for S, Mn, Al, and N (a, b, c, d) utilizes EDS to examine an AlN precipitate alongside a MnS precipitate in alloy B21A188 after annealing at 1100 °C for 1800 s.

Figure 5 shows the chemical analysis by EDS of AlN and MnS precipitates located along each other in the alloy B21A188 after annealing at 1180 °C for 1800 s. The EDS mappings (a, b, c, d) in Figure 4 give more details on the distribution of Al, N, Mn and S atoms, showing the actual size of the precipitate and the positioning of the two precipitates along each other. A close nesting between MnS and AlN is evident. AlN precipitates are found in the size range of approx. 100 nm, which is close to the lower resolution limit for PA up to 1 μ m. A clear dependence of the AlN particle size on the Al fraction in the alloy is observed, with AlN smaller than 300 nm in alloy B21Al35 and reaching particle diameters larger than 1 μ m in alloy B21A188. Co-precipitation of AlN and MnS in microalloyed steel has been reported by [27,76] and is also observed in this study, see Figure 5. AlN precipitates in the size of 100 nm are not found with a solubility of Mn, as shown in Figure 4.

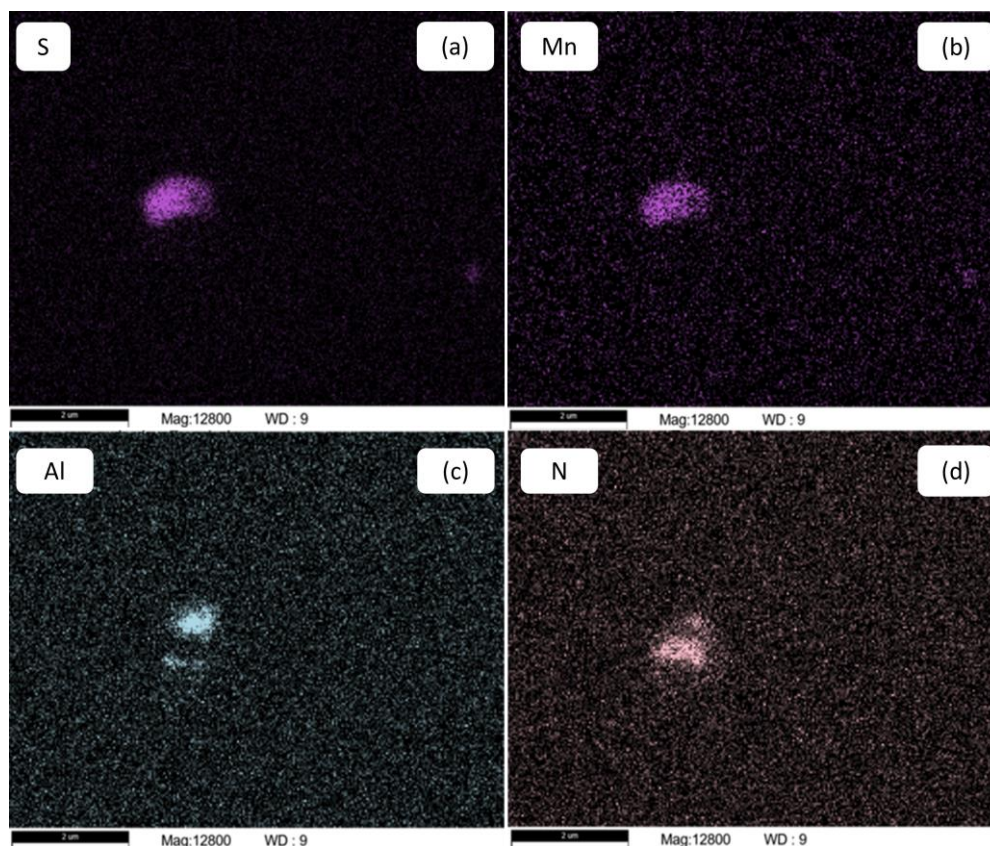


Figure 5. Chemical analysis mapping for S, Mn, Al, and N (a, b, c, d) utilizes EDS to examine an AlN precipitate alongside a MnS precipitate in alloy B21Al88 after annealing at 1180 °C for 1800 s.

The occurrence of two distinct peaks in the distribution of AlN diameters is evident. As demonstrated in Figure 4, the formation of small AlN with diameters of approximately 100 nm occurs during processing at lower temperatures. In contrast, the formation of larger AlN occurs at higher temperatures, with the nucleation being initiated at these elevated temperatures. As the aluminum composition increases, the solvus temperature of the aluminum nitride (AlN) also increases. Consequently, the size of the particles increases as well, due to the higher diffusivities that occur at higher temperatures.

Figure 6 shows exemplarily a corresponding EDS/WDS analysis of a BN precipitate (b), typically located at an austenite grain boundary, in alloy Al36B44 after annealing for 1800 s at 1200 °C. The spectrum (a) from the WDS analysis shows the presence of both B and N.

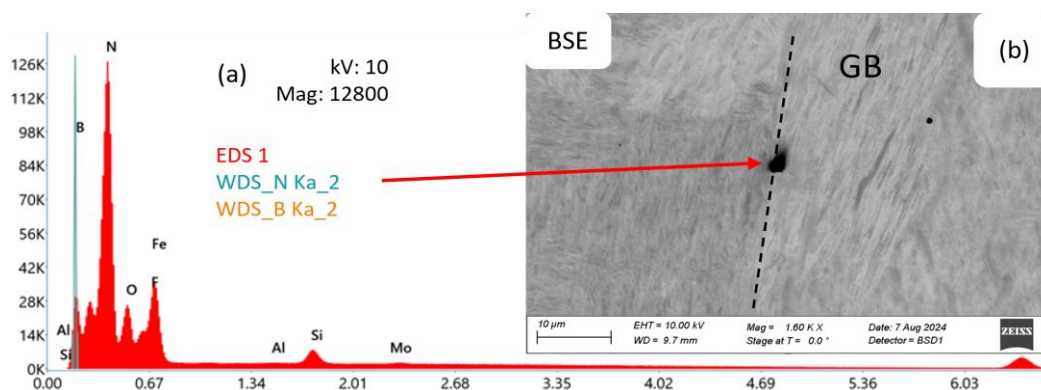


Figure 6. SEM-BSE image of a BN precipitate (b) at a grain boundary (GB). Chemical analysis of a BN precipitate using EDS and WDS (a) for alloy Al36B44 after annealing for 1800 s at 1200 °C. B is detected using WDS.

From the analysis in the SEM, it can be concluded that BN precipitates appear as roundish features in the range of 1 μm - 5 μm and are predominantly nucleated at grain boundaries, as reported in the literature [7,31].

Protection of boron from nitrogen by excess aluminum is controversial. According to the review by Sharma et al. [7], it is believed that AlN dissolves at high temperatures, allowing the N to recombine with B. However, this study shows that AlN remains stable at high temperatures. In a system with 21 wt.-ppm B and 83 wt.-ppm N, an Al fraction greater than 0.09 wt.% is sufficient to completely suppress BN. As a rule of thumb for the preferential precipitation of AlN over the formation of BN, an Al/N ratio of 20 is found for a B fraction of 21 wt.-ppm.

4.2.2. Pseudo-Binary Fe-Al and Fe-B Phase Diagram Within the Fe-N-C-Al-B System

As illustrated in Figure 7, the pseudo-binary Fe-Al diagram for the system Fe-C-N-Al-B with 0.5 wt.-% C, 79 wt.-ppm N, and 21 wt.-ppm B for the austenite region is calculated with the thermodynamic database ME-Fe_CDLIPE2.0.2.tdb [17].

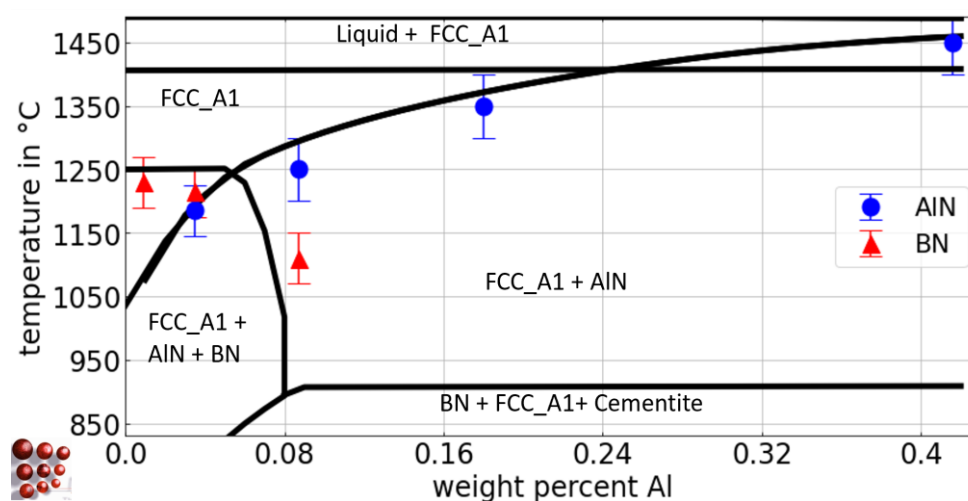


Figure 7. Calculated pseudo-binary Fe-Al phase diagram with 0.5 wt.-% C, 79 wt.- ppm N, and 21 wt.-ppm B for the austenite region of the Fe-C-N-Al-B system, ME-Fe_CDLIPE2.0.2.tdb [17]. The blue circles and the red triangles mark the experimental results with error bars for T_{sol} of AlN and BN for the alloys B21Al0, B19Al35, B21Al88, B21Al180, and B21Al416, respectively. (For interpretation of the references to color in this figure legend, the reader is referred to the Web version of this article.)

The blue circles and red triangles represent the experimental results from Section 4.2.1 for T_{sol} of AlN and BN, respectively. T_{sol} of BN for the alloys B21Al0, B19Al35, and B21Al88 lies within a narrow range, as evidenced by the experimental results. From a thermodynamic perspective, the higher affinity of boron for nitrogen compared to aluminum [8,77] elucidates the amount of aluminum necessary to restrict the solubility of BN in austenite [7], with approximately 0.09 wt.-% required to entirely impede BN formation. Figure 8 shows the pseudo-binary Fe-B diagram for the Fe-rich side of the system Fe-C-N-Al-B with 0.5 wt.-% C, 79 wt.- ppm N, and 0.03 wt.-% Al for the austenite region. These calculations are derived from the thermodynamic database ME-Fe_CDLIPE2.0.2.tdb [17]. The blue circles and red triangles represent the experimental results from Section 4.2.1 for T_{sol} of AlN and BN, respectively.

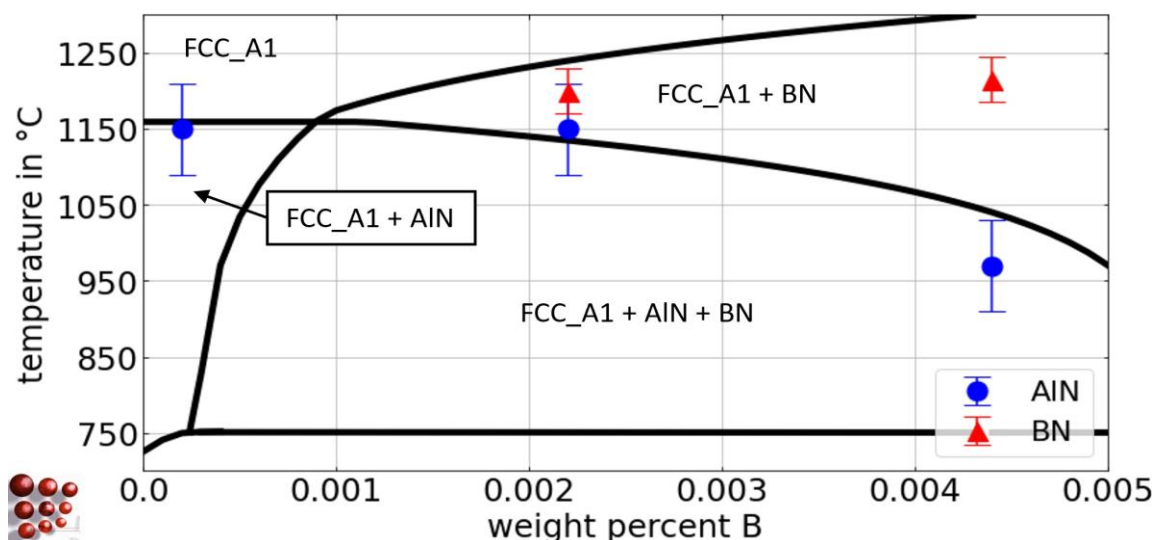


Figure 8. Calculated pseudo-binary Fe-B phase diagram with 0.5 wt.-% C, 79 wt.-ppm N, and 0.03 wt.-% Al for the austenite region of the Fe-C-N-Al-B system, ME-Fe_CDLIPE2.0.2.tdb [17]. The blue circles and the red triangles mark the experimental results with error bars for T_{sol} of AIN and BN for the alloys Al29B0, Al29B22, and Al36B44. (For interpretation of the references to color in this figure legend, the reader is referred to the Web version of this article.).

As the boron fraction increases, the stability of BN begins to manifest at approximately 4 wt.-ppm B. The presence of competing phases, AIN and BN, leads to a reduction in AIN precipitates with an increase in boron content, owing to the formation of BN. At B concentrations greater than 50 wt.-ppm, AIN is completely dissolved.

This work definitively shows that AIN and BN are competing phases. An increase in either aluminum or boron content favors the formation of the corresponding phase, AIN or BN. The BN phase is generally more stable than AIN due to the strong affinity of boron for nitrogen, depending on the relative concentrations of Al, B, and N.

4.3. Interrelation of AIN, BN and TiN Within Fe-C-N-Al-B-Ti

4.3.1. Experiment

In Table 5, the experimental findings concerning the T_{sol} of the precipitate phases AIN, BN, and TiN for the alloys exhibiting variable titanium concentrations are presented. The data shows the strong affinity of Ti for N, as evidenced by the observation that a mere of 0.03 wt.-% Ti is enough to entirely impede the formation of AIN and BN. This phenomenon, consequently, facilitates the advantageous effect of safeguarding B for the desired „boron-effect“ outcome. There is no evidence of mixing between the AIN, BN, and TiN phases in the EDS mapping. The determination of T_{sol} for TiN is achieved through the integration of thermodynamic equilibrium simulation with experimental evaluation. In the case of alloy Al36B25Ti0, no TiN are detected, whereas in all other alloys containing Ti, TiN are found. The high solubility temperature of TiN, which is approximately 1430°C or higher, renders dissolution experiments in the dilatometer unfeasible. In Figure 9, an exemplary corresponding EDS analysis of a TiN precipitate in alloy Al42B38Ti30 after annealing at 1300 °C for 1200 s is shown, yielding a spectrum (a) that substantiates the presence of Ti and N. The EDS mappings (b, c, d, and e) provide further insight into the distribution of the Ti, N, Fe, and C atoms, respectively, and demonstrate the actual size of the precipitate. The size of the detected TiN precipitates ranges from 100 nm (lower detection limit) to several μm .

Table 5. Experimental and computed T_{sol} of AIN, BN, and TiN in the Fe-C-N-Al-B-Ti system. The values for TiN are taken from thermodynamic equilibrium simulation.

Alloy	Al	B	Ti	N	T_{sol} AIN	T_{sol} BN	T_{sol} AIN	T_{sol} BN	T_{sol} TiN
-------	----	---	----	---	---------------	--------------	---------------	--------------	---------------

	in wt.-%				experiment in °C		simulation in °C		
Al36B25Ti0	0.036	0.0025	0.000	0.0069	1140±20	1230±20	1170	1240	-
Al38B36Ti20	0.038	0.0036	0.020	0.0052	-	1120±20	-	1100	1430±20
Al42B38Ti30	0.042	0.0038	0.030	0.0045	-	-	-	-	1440±20
Al44B39Ti42	0.044	0.0039	0.042	0.0042	-	-	-	-	1450±20

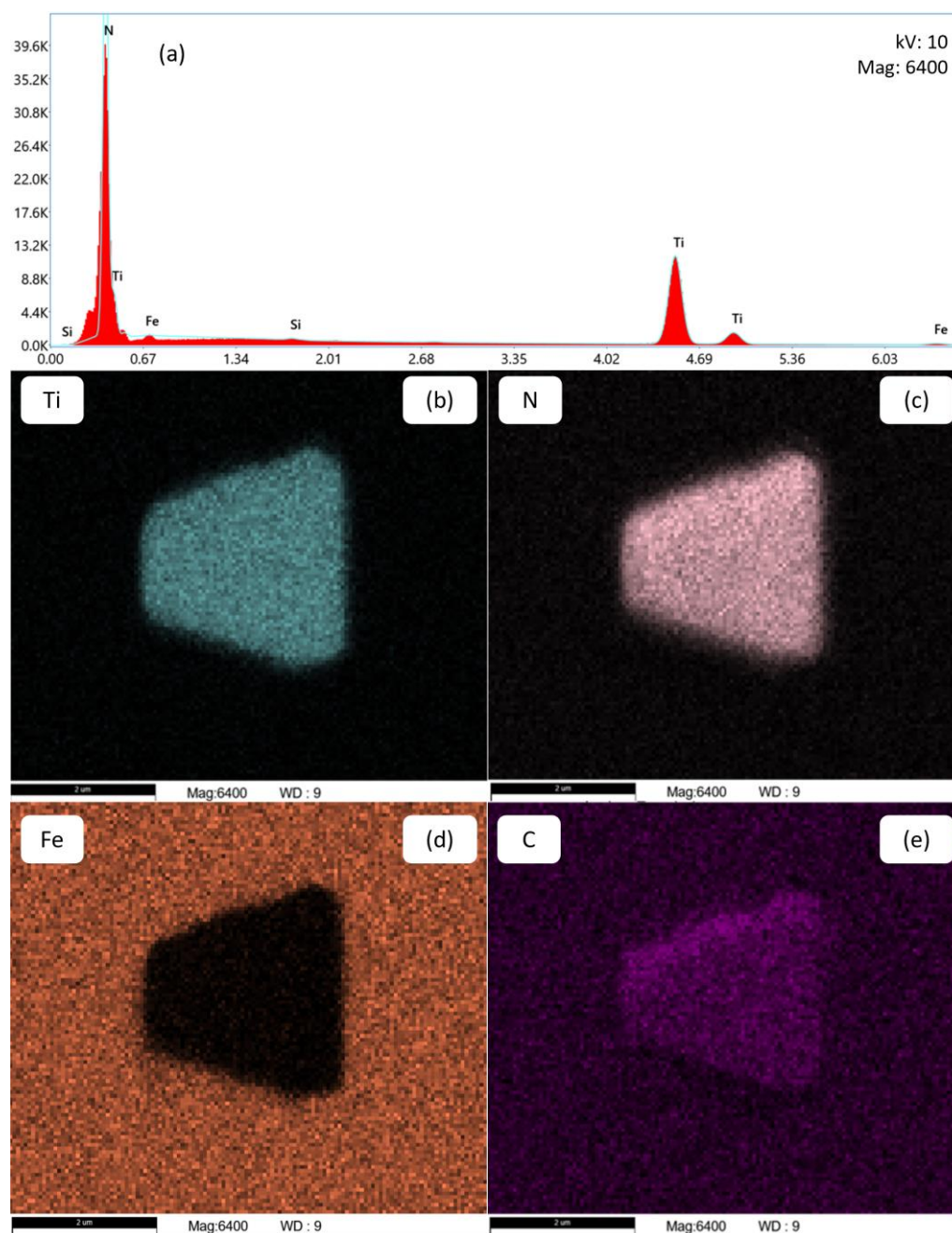


Figure 9. Chemical analysis of a TiN precipitate using EDS (a) in alloy Al42B38Ti30 after annealing at 1300 °C for 1200 s. The EDS mappings in b, c, d, and e show the distribution of Ti, N, Fe, and C atoms, respectively.

As illustrated in Figure 10, the results of the particle analysis for alloy Al42B38Ti30 after annealing at 1000 °C for 10000 s indicate the presence of TiN and MnS. The blue and red dots, respectively, denote the positions of these two phases. The precipitate size in the plot is multiplied by 20 to enhance the visibility of the particles. The absence of BN and AlN in the present measurement further suggests that AlN and BN are not stable within the alloy and annealing temperature under investigation. The diameter of titanium nitride (TiN) is distributed over a wide range, from a mere

hundred nanometers to several micrometers. The formation of large TiN precipitates is hypothesized to occur at elevated temperatures or primarily from the liquid phase [78]. Small TiN are thought to nucleate as secondary precipitates from the solid state at lower temperatures during the subsequent production process.

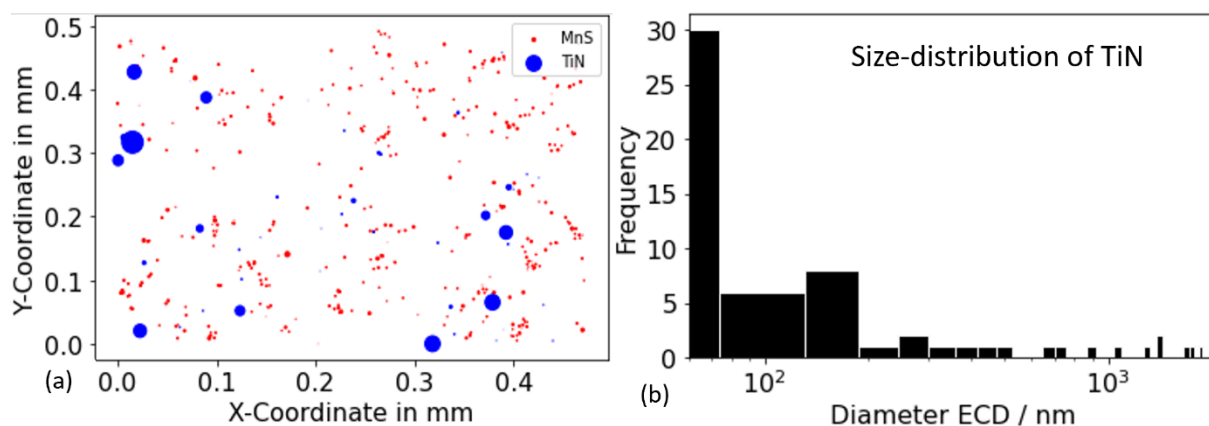


Figure 10. Results of particle analysis for alloy Al42B38Ti30 after annealing at 1000 °C for 10000 s (a) Position of the TiN (blue) and MnS (red) precipitates. The precipitate size in the plot is multiplied by 20 to make the particles more easily visible. (b) Distribution of the TiN precipitates diameter.

Figure 11 shows the resulting austenite grain size after annealing at 1000°C for 500 s and 10000 s, respectively. A profound bimodal grain size distribution can be observed, indicating the abnormal grain growth behavior. This behavior is explained by the absence of grain boundary pinning AlN precipitates. A similar effect is reported by Roy et al. [37] and Monschein et al. [35] in HSLA steel, where the dissolution of second phase particles at higher soaking temperatures is reported to allow AGG. In the alloys without Ti alloying, AGG was not observed, further supporting the theory that the lack of AlN leads to AGG.

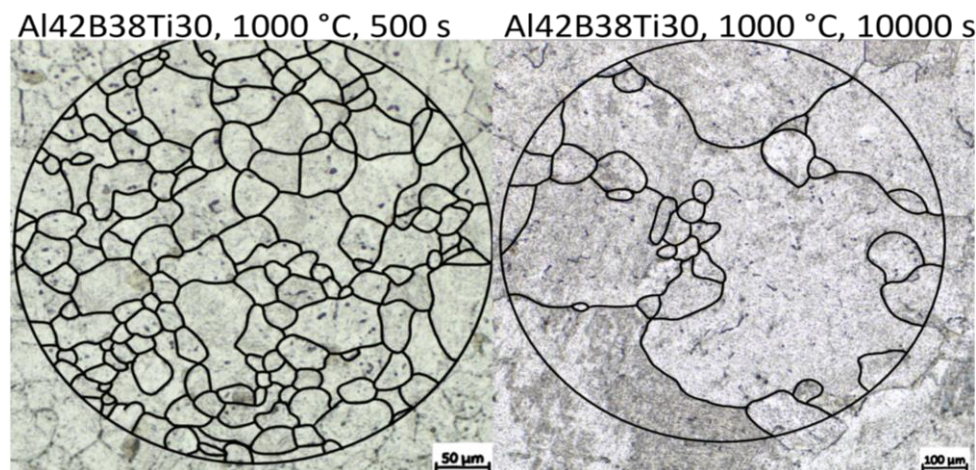


Figure 11. Comparison of the resulting austenite grain size for alloy Al42B38Ti30 after annealing at 1000 °C for 500 s and 10000 s, respectively. Etching is performed with PM1998 [75]. Black lines are drawn to highlight the PAGB.

4.3.2. Pseudo-Binary Fe-Ti Phase Diagram Within the Fe-N-C-Al-B-Ti System

Figure 12 shows a calculated pseudo-binary Fe-Ti diagram for the Fe-rich side with 0.5 wt.-% C, 79 wt.-ppm N, 0.03 wt.-% Al, and 36 wt.-ppm B for the austenite region of the Fe-C-N-Al-B-Ti system, using the thermodynamic database ME-Fe_CDLIPE2.0.2.tdb [17]. The blue circles, red triangles and green stars represent the experimental results from Section 4.2.1 for T_{sol} of TiN, BN, and AlN, respectively. However, small discrepancies between simulation results and experimental data are

observed, which are attributed to experimental evaluation uncertainties, primarily due to resolution limits, and the complex interactions with numerous degrees of freedom in the multicomponent system. In fact, calibration of such interactions can be done, but we prefer to accept deviations due to the high doubt of the appropriate physical base for their modeling. The collective analysis of the simulation results indicates a reasonable agreement between the simulations and the experimental observations, suggesting a satisfactory overall outcome.

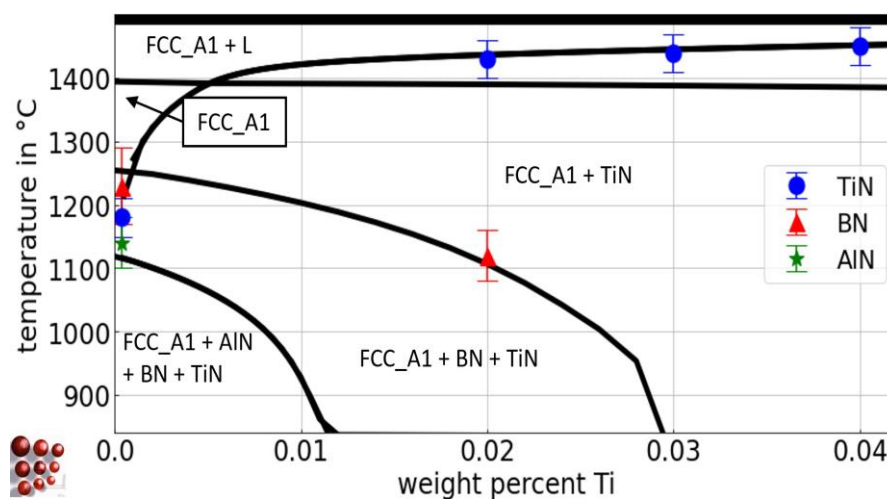


Figure 12. Calculated pseudo-binary Fe-Ti phase diagram with 0.5 wt.-% C, 79 wt.-ppm N, 0.03 wt.-% Al, and 36 wt.-ppm B for the austenite region of the Fe-C-N-Al-B-Ti system, ME-Fe_CDLIPE2.0.2.tdb [17]. The blue circles, the red triangles, and green stars mark the experimental results with error bars for T_{sol} of TiN, BN, and AlN for the alloys Al36B25Ti0, Al38B36Ti20, Al42B38Ti30, and Al44B39Ti42. (For interpretation of the references to color in this figure legend, the reader is referred to the Web version of this article.).

5. Summary

Our experimental investigation in high-purity vacuum induction melted alloys confirms that Ti, B, and Al exhibit decreasing affinities to nitrogen, forming nitrides in microalloyed steel. In the competitive interaction with aluminum, in the Fe-C-N-Al-B system, increasing the Al content to 0.09 wt.-% effectively inhibits the formation of BN, in contrast to previous understanding of the negligible protective role of Al at high temperatures. AlN is found to co-precipitate with MnS. Titanium proves to be very effective in blocking the formation of other nitrides. The presence of 0.02 wt.-% Ti completely blocks the formation of AlN and shifts T_{sol} of BN by 150 °C. The addition of 0.03 wt.-% Ti is sufficient to suppress the formation of both BN and AlN. By integrating available binary and ternary descriptions into a thermodynamic database, we predict the stabilities of the multicomponent system Fe-C-N-Al-B-Ti. Overall, considering the simulation results for nitride phase boundaries, the outcomes are satisfying, as reflected by a reasonable agreement between the simulations and experimental observations. This further confirms the control by the thermodynamics of binary and ternary subsystems, since the extension to quaternaries, quinary and the multi-component steel system studied has been considered ideal, and the applicability of the steel database, being optimized by new experimental data in the Fe-rich corner for dilute microalloyed steel is confirmed.

In the alloys with even a small amount of Ti, abnormal grain growth behavior is observed. This inhomogeneous grain growth is attributed to the absence of AlN precipitates, which are known to retard grain boundary movement.

Author Contributions: Conceptualization, M.F. and E.P.-K.; methodology, M.F., C.S., E.P.-K.; software, M.F., E.P.-K.; investigation, M.F., C.S.; writing—original draft preparation, M.F.; writing—review and editing, M.F., S.Z., C.S., and E.P.-K.; visualization, M.F.; supervision, E.P.-K. All authors have read and agreed to the published version of the manuscript.

Funding: This research was funded by Christian Doppler Forschungsgesellschaft in the framework of the CD-Laboratory of Interfaces and Precipitation Engineering (CDL-IPE).

Acknowledgments: The financial support from the Austrian Federal Ministry for Digital and Economic Affairs and the National Foundation for Research, Technology, and Development is gratefully acknowledged. The authors acknowledge TU Wien Bibliothek for financial support through its Open Access Funding Programme. The financial support, as well as the provision of sample material by voestalpine Forschungsservicegesellschaft, is gratefully acknowledged by the authors.

Conflicts of Interest: The authors declare no conflict of interest. The funders had no role in the design of the study, in the collection, analyses, or interpretation of data, in the writing of the manuscript, or in the decision to publish the results.

Data availability: Data will be made available on request

References

1. Baker TN (2016) Microalloyed Steels. *Ironmaking & Steelmaking*, Taylor & Francis 43(4): 264–307. doi: 10.1179/1743281215y.0000000063
2. Costa e Silva A (2020) Challenges and opportunities in thermodynamic and kinetic modeling microalloyed HSLA steels using computational thermodynamics. *Calphad* 68: 101720. doi: 10.1016/j.calphad.2019.101720
3. HABU R, MIYATA M, TAMUKAI S et al. (1983) Improvement of Hardenability of Steel Containing Aluminum and Boron by Double Quenching. *ISIJ International* 23(2): 176–183. doi: 10.2355/isijinternational1966.23.176
4. KAWAMURA K, OTSUBO T, FURUKAWA T (1976) Relationship between the Hardenability of Steel and the “Effective Boron” in Steel. *ISIJ Int.* 16(10): 545–550. doi: 10.2355/isijinternational1966.16.545
5. McMahon CJ (1980) The role of solute segregation in promoting the hardenability of steel. *Metall Trans A* 11(3): 531–535. doi: 10.1007/BF02654577
6. Wipp D (2021) Boron Influence on Microstructural Evolution and Mechanical Properties in Micro-Alloyed Carbon Steels : Precipitation and Segregation Behavior. Dissertation, Technische Universität Wien
7. Sharma M, Ortlepp I, Bleck W (2019) Boron in Heat-Treatable Steels: A Review. *steel research international* 90(11): 1900133. doi: 10.1002/srin.201900133
8. Wang WS, Zhu HY, Sun J et al. (2019) Thermodynamic analysis of BN, AlN AND TiN Precipitation in boron-bearing steel. *Metallurgija* 58(3-4): 199–202
9. Baker TN (2019) Titanium Microalloyed Steels. *Ironmaking & Steelmaking* 46(1): 1–55. doi: 10.1080/03019233.2018.1446496
10. Wilson FG, Gladman T (1988) Aluminium Nitride in Steel. *International Materials Reviews* 33(1): 221–286. doi: 10.1179/imr.1988.33.1.221
11. Kaufman L, Bernstein H (1970) Computer calculation of phase diagrams. With special reference to refractory metals. Academic Press Inc, New York
12. P Gustafson (1985) A thermodynamic evaluation of the Fe-C system. *Calphad*: 259–267
13. Frisk K (1991) A thermodynamic evaluation of the Cr-N, Fe-N, Mo-N and Cr-Mo-N systems. *Calphad* 15(1): 79–106. doi: 10.1016/0364-5916(91)90028-I
14. Miettinen J, Visuri V-V, Fabritius T et al. (2020) Thermodynamic Description of Ternary Fe-B-X Systems. Part 7: Fe-B-C. *Archives of Metallurgy and Materials* Vol. 65, iss. 2: 923–933. doi: 10.24425/amm.2020.132840
15. Lee B-J (2001) Thermodynamic assessment of the Fe-Nb-Ti-C-N system. *Metallurgical and Materials Transactions A* 32(10): 2423–2439. doi: 10.1007/s11661-001-0033-x
16. Chin K-G, Lee H-J, Kwak J-H et al. (2010) Thermodynamic calculation on the stability of (Fe,Mn)3AlC carbide in high aluminum steels. *Journal of Alloys and Compounds* 505(1): 217–223. doi: 10.1016/j.jallcom.2010.06.032
17. E. Povoden-Karadeniz (Ed.) (2025) Thermodynamic Database “ME-Fe_CDLIPE2.0.2.tdb”,
18. Najafkhani F, Kheiri S, Pourbahari B et al. Recent Advances in the Kinetics of Normal/Abnormal Grain Growth: A Review. *1644-9665* 21(1): 1–20. doi: 10.1007/s43452-021-00185-8

19. Rios PR, Fonseca GS (2010) Grain Boundary Pinning by Particles. *Materials Science Forum* 638-642: 3907–3912. doi: 10.4028/www.scientific.net/MSF.638-642.3907
20. Radis R, Kozeschnik E (2010) Kinetics of AlN Precipitation in Microalloyed Steel. *Modelling and Simulation in Materials Science and Engineering* 18(5): 55003. doi: 10.1088/0965-0393/18/5/055003
21. Wriedt HA The Al-N (Aluminum-Nitrogen) System. *Bulletin of Alloy Phase diagrams* 1986(4): 329–333. doi: 10.1007/bf02873001
22. Bruls RJ, Hintzen HT, With G de et al. (2001) The temperature dependence of the Grueneisen parameters of MgSiN₂, AlN. *Journal of Physics and Chemistry of Solids* 62(4): 783–792. doi: 10.1016/S0022-3697(00)00258-4
23. Lu X-G, Selleby M, Sundman B (2005) Assessments of molar volume and thermal expansion for selected bcc, fcc and hcp metallic elements. *Calphad* 29(1): 68–89. doi: 10.1016/j.calphad.2005.05.001
24. Sennour M, Esnouf C (2003) Contribution of Advanced Microscopy Techniques to Nano-Precipitates Characterization: Case of AlN Precipitation in Low-Carbon Steel. *Acta Materialia* 51(4): 943–957. doi: 10.1016/s1359-6454(02)00498-6
25. Gao N, Baker TN (1998) Austenite Grain Growth Behaviour of Microalloyed Al-V-N and Al-V-Ti-N Steels. *ISIJ Int.* 38(7): 744–751. doi: 10.2355/isijinternational.38.744
26. Chen Y, Wang Y, Zhao A (2012) Precipitation of AlN and MnS in Low Carbon Aluminium-Killed Steel. *J. Iron Steel Res. Int.* 19(4): 51–56. doi: 10.1016/S1006-706X(12)60087-9
27. Führer M, Zamberger S, Povoden-Karadeniz E (2025) Experimental determination of AlN in microalloyed steel and thermodynamic analysis. *Calphad* 88: 102790. doi: 10.1016/j.calphad.2024.102790
28. Massardier V, Guétaz V, Merlin J et al. Kinetic and Microstructural Study of Aluminium Nitride Precipitation in a Low Carbon Aluminium-Killed Steel. *Materials Science and Engineering: A* 2003(1-2): 299–310. doi: 10.1016/s0921-5093(03)00080-7
29. Pearson, W. B. , Villars, P. , Calvert, L. D. (1986) *Pearson's handbook of crystallographic data for intermetallic phases*. Cambridge
30. Suzuki S, Tanino M (2007) Role of Grain Boundary Segregation in Austenite Decomposition of Low-Alloyed Steel. *Trans. Tech. Publ.* 558-559: 965–970. doi: 10.4028/www.scientific.net/MSF.558-559.965
31. Sakuraya K, Okada H, Abe F (2006) Influence of Heat Treatment on Formation Behavior of Boron Nitride Inclusions in P122 Heat Resistant Steel. *1347-5460* 46(11): 1712–1719. doi: 10.2355/isijinternational.46.1712
32. Jonsson S (1998) Assessment of the Fe-Ti-C system, calculation of the Fe-TiN system, and prediction of the solubility limit of Ti(C,N) in liquid Fe. *Metall Mater Trans B* 29(2): 371–384. doi: 10.1007/s11663-998-0114-y
33. (1990) High-Strength Structural and High-Strength Low-Alloy Steels. *ASM Metals Handbook*. 10th ed. Vol. 1. p. 403–423. In: Properties and selection: irons, steels and high performance alloys
34. Gontijo M, Chakraborty A, Webster RF et al. (2022) Thermomechanical and Microstructural Analysis of the Influence of B- and Ti-Content on the Hot Ductility Behavior of Microalloyed Steels. *Metals* 12(11): 1808. doi: 10.3390/met12111808
35. Monschein S, Ragger KS, Zügner D et al. (2022) Influence of the Ti Content on the Grain Stability and the Recrystallization Behavior of Nb-Alloyed High-Strength Low-Alloyed Steels. *steel research international* 93(7): 2200094. doi: 10.1002/srin.202200094
36. Su C, Zhao G, Xiao H et al. (2018) Abnormal Grain Growth of Hi-B Steel in the Secondary Recrystallization. *Metallogr. Microstruct. Anal.* 7(5): 608–617. doi: 10.1007/s13632-018-0467-9
37. Roy S, Karmakar A, Mukherjee S et al. (2014) Effect of starting microstructure on austenite grain sizes developed after reheating of HSLA steel. *Materials Science and Technology* 30(10): 1142–1153. doi: 10.1179/1743284713Y.0000000385
38. Lang D, Povoden-Karadeniz E, Schatte J et al. (2017) Thermodynamic evaluation of the Mo-rich corner of the Mo-Hf-C system including O impurities. *Journal of Alloys and Compounds* 695: 372–381. doi: 10.1016/j.jallcom.2016.10.227
39. Saunders N, Miodownik AP (1998) *CALPHAD (Calculation of Phase Diagrams): A Comprehensive Guide*, Transferred to digital print. Pergamon Materials Series. Pergamon
40. Dinsdale AT (1991) *SGTE Data for Pure Elements*. *Calphad* 15(4): 317–425. doi: 10.1016/0364-5916(91)90030-n

41. Chipman J (1972) Thermodynamics and phase diagram of the Fe-C system. *Metall Trans* 3(1): 55–64. doi: 10.1007/BF02680585
42. Göhring H, Leineweber A, Mittemeijer EJ (2016) A thermodynamic model for non-stoichiometric cementite; the Fe–C phase diagram. *Calphad* 52: 38–46. doi: 10.1016/j.calphad.2015.10.014
43. Naraghi R, Selleby M, Ågren J (2014) Thermodynamics of stable and metastable structures in Fe–C system. *Calphad* 46: 148–158. doi: 10.1016/j.calphad.2014.03.004
44. Hallstedt B, Djurovic D, Appen J von et al. (2010) Thermodynamic properties of cementite . *Calphad* 34(1): 129–133. doi: 10.1016/j.calphad.2010.01.004
45. van Rompaey T, Hari Kumar K, Wollants P (2002) Thermodynamic optimization of the B–Fe system. *Journal of Alloys and Compounds* 334(1-2): 173–181. doi: 10.1016/S0925-8388(01)01777-7
46. T.G. Chart (1981). *Comm. Comm. Eur.*, 7210-CA/3/303
47. T.B. Massalski (Ed.) (1990) *Binary Alloys Phase Diagrams*, 2nd Edition. ASM International, Metals Park, OH
48. O. Kubaschewski (1982) *Iron–Binary Phase Diagrams*. Springer Verlag, Berlin
49. Hallemans B, Wollants P, Roos JR (1994) Thermodynamic Reassessment and Calculation of the Fe-B Phase Diagram. *International Journal of Materials Research* 85(10): 676–682. doi: 10.1515/ijmr-1994-851002
50. Ohtani H, Hasebe M, ISHIDA K et al. (1988) Calculation of Fe-C-B ternary phase diagram. *ISIJ Int.* 28(12): 1043–1050. doi: 10.2355/isijinternational1966.28.1043
51. Kaufman L, Uhrenius B, Birnie D et al. (1984) Coupled pair potential, thermochemical and phase diagram data for transition metal binary systems-VII. *Calphad* 8(1): 25–66. doi: 10.1016/0364-5916(84)90026-9
52. Lucci A, Della Gatta G, Venturello G (1969) On the Solubility of Boron in High-Purity Alpha-Iron. *Metal Science Journal* 3(1): 14–17. doi: 10.1179/msc.1969.3.1.14
53. Brodowsky H, Wernicke H-J (1984) Activity coefficients and the alpha-gamma transition lines in fe-b alloys. *Calphad* 8(2): 159–162. doi: 10.1016/0364-5916(84)90007-5
54. Brown A, Garnish JD, Honeycombe RWK (1974) The Distribution of Boron in Pure Iron. *Metal Science* 8(1): 317–324. doi: 10.1179/msc.1974.8.1.317
55. Raghavan V (1993) B-Fe-N (boron-iron-nitrogen). *JPE* 14(5): 619–620. doi: 10.1007/BF02669145
56. Tomashik V (2008) Boron – Iron – Nitrogen. iron systems: phase diagrams, crystallographic and thermodynamic data. *Landolt-Börnstein - Group IV Physical Chemistry*: 457–471. doi: 10.1007/978-3-540-69761-9_20
57. Fountain RW, Chipman J (1962) SOLUBILITY AND PRECIPITATION OF BORON NITRIDE IN IRON-BORON ALLOYS. Union Carbide Metals Co., Niagara Falls, N.Y. Vol: 224
58. Markus Führer, Sabine Zamberger, Yao Shan, Lukas Helml, Kiranbabu Srikakulapu, Ronald Schnitzer, Ernst Kozeschnik, Erwin Povoden-Karadeniz (2025) Influence of boron grain boundary segregation on the thermodynamics of the Fe-C-B-N system [unpublished manuscript]. Institute of materials science and technology, TU Wien
59. N. Saunders (1998) COST 507: Thermochemical database for light metal alloys Vol. 2, pp 23-27
60. Jacob A, Sobotka E, Povoden-Karadeniz E (2025) Thermodynamic modeling of multicomponent MX phases (M= Nb,Ti,V; X=C,N) in steel. *Calphad* 88: 102795. doi: 10.1016/j.calphad.2024.102795
61. E. Povoden-Karadeniz (2023) mc_fe_v2.061. https://www.matcalc.at/images/stories/Download/Database/mc_fe_v2061.tdb
62. Hillert M, Jonsson S (1992) An Assessment of the Al- Fe- N System. *Metall Trans A* 23(11): 3141–3149. doi: 10.1007/bf02646133
63. Miettinen J, Vassilev G (2014) Thermodynamic Description of Ternary Fe-B-X Systems. Part 1: Fe-B-Cr. *Archives of Metallurgy and Materials* 59(2): 601–607. doi: 10.2478/amm-2014-0099
64. M. Seierstein (1998) System Al–Fe. COST507, Thermochemical Database for Light Metal Alloys, Vol 2, I. Ansara, A.T. Dinsdale, and M.H. Rand. European Commission, Luxembourg, p. 234. Office for Official Publications
65. Witusiewicz VT, Bondar AA, Hecht U et al. (2008) The Al–B–Nb–Ti system. *Journal of Alloys and Compounds* 465(1-2): 64–77. doi: 10.1016/j.jallcom.2007.10.061
66. Am S Maneschi B (1966) Analysis of nitrides in boron steels by extraction of nonmetallic phases. *MET ITAL.*

67. E. T. Turkdogan (1987) Causes and effects of nitride and carbonitride precipitation in HSLA steels in relation to continuous casting. In 70th Steelmaking Conference Proceedings, Pittsburgh, PA, March 29 - April 1
68. Sridar S, Kumar R, Kumar H (2019) Thermodynamic Modelling of Al-B-N System. *Calphad* 65: 291–298. doi: 10.1016/j.calphad.2019.03.008
69. H. Wen HL (1998) Thermochemical database for light metal alloys, in: I. Ansara, A.T. Dinsdale, M.H. Rand (Eds.), COST507. European Communities, Luxembourg(Vol. 2, System B-N.): pp. 65–68 Ch.
70. Thermo-Calc Software (2023) CALPHAD Methodology - Thermo-Calc Software. <https://thermocalc.com/about-us/methodology/the-calphad-methodology/>. Accessed 05 Apr 2024
71. Dworkin AS, Sasmor DJ, van Artsdalen ER (1954) The Thermodynamics of Boron Nitride; Low-Temperature Heat Capacity and Entropy; Heats of Combustion and Formation. *J. Chem. Phys.* 22(5): 837–842. doi: 10.1063/1.1740199
72. LECO Corporation (2025) LECO. <https://de.leco.com/>. Accessed 07 Feb 2025
73. Law CA (1999) Treatise of Petroleum Geology / Handbook of Petroleum Geology: Exploring for Oil and Gas Traps. Chapter 6: Evaluating Source Rocks. AAPG Special Volumes
74. (2024) Lambda WDS Spectrometers | EDAX. <https://www.edax.com/products/wds/lambda-wds-analysis-system>. Accessed 08 Aug 2024
75. Schacht E, Richter J (1998) Erfahrungen mit Ätzmitteln zum Nachweis der ehemaligen Austenitkorgrenzen in Stählen / Experiences with Etching Reagents to Show Former Austenite Grain Boundaries in Steels. *Ätzmittel* 35(7): 384–395. doi: 10.1515/pm-1998-350706
76. Lückl M Kinetics Simulation of MnS Precipitation in Electrical Steel. *1869-344X* 87(3): 271–275
77. Wang Y-N, Bao Y-P, Wang M et al. (2013) Basic Research on Precipitation and Control of BN Inclusions in Steel. *Metall Mater Trans B* 44(5): 1144–1154. doi: 10.1007/s11663-013-9881-1
78. Schneider A, Stallybrass C, Konrad J et al. (2008) Formation of primary TiN precipitates during solidification of microalloyed steels – Scheil versus DICTRA simulations. *International Journal of Materials Research* 99(6): 674–679. doi: 10.3139/146.101689

Disclaimer/Publisher's Note: The statements, opinions and data contained in all publications are solely those of the individual author(s) and contributor(s) and not of MDPI and/or the editor(s). MDPI and/or the editor(s) disclaim responsibility for any injury to people or property resulting from any ideas, methods, instructions or products referred to in the content.